An experimental investigation of hydrodynamics of a fixed OWC Wave Energy Converter

De-Zhi Ning[1*], Rong-Quan Wang[1], Qing-Ping Zou[2], Bin Teng[1]

1.State Key Laboratory of Coastal and Offshore Engineering, Dalian University of Technology, Dalian, 116024, China; 2.Department of Civil and Environmental Engineering, University of Maine, Orono, ME 04469, USA

Abstract

The hydrodynamic performance of a fixed Oscillating Water Column (OWC) wave energy device under various wave conditions and geometric parameters was tested experimentally in a wave flume. The measured water surface elevation at the chamber center, the air pressure in the chamber of the OWC device and the hydrodynamic efficiency are compared well with the published numerical model results in Ref. [22]. Then the effects of various parameters including incident wave amplitude, the chamber width, the front wall draught, the orifice scale and the bottom slope on the hydrodynamic efficiency of the OWC device were investigated. It is found that the opening ratio ε ($\varepsilon = S_0/S$, where S_0 and S are the cross-sectional areas of the orifice and the air chamber, respectively) has a significant influence on the maximum hydrodynamic efficiency of the OWC device. The optimal efficiency occurs at the opening ratio of ε=0.66%. Although bottom slope has little influence on the resonant frequency, the optimal hydrodynamic efficiency increases with the increase of bottom slope. A proper bottom slope can provide a work space in the OWC chamber almost independent on the sea wave conditions. The spatial variation of the water surface inside and outside the chamber was also examined. And the results indicate that the water motion is highly dependent on the relative wave length λ/B (where λ is the wave length and B is the chamber width). Seiching phenomenon is triggered when λ/B=2 at which the hydrodynamic efficiency is close to zero.

* Corresponding author. Tel: +86 41184708267
Email-address: dzning@dlut.edu.cn

Key words: OWC; Wave energy; Model testing; Hydrodynamic efficiency; Water motion.

1. Introduction

To cope with the increasing costs of fossil fuels and the environmental problems derived from the extraction and the use of fossil fuels, renewable energy sources are believed to play a more and more important role to mitigate these effects [1]. Wave energy is certainly a significant component of the renewable energy [2] due to its high energy density [3] and less negative environmental impact [4, 5]. More than one thousand wave energy converter patents had been registered by 1980 and the number has increased markedly since then [6], in which the OWC device has been extensively studied and implemented due to its mechanical and structural simplicity [7]. Generally, a land-fixed OWC device consists of two parts: a partially submerged land back chamber and an open below the mean sea level. They are used to trap a column of air above the free surface. As the waves impinge on the device, the oscillating motion of the internal water free surface makes the air to flow through a turbine that drives an electrical generator [8]. A number of full sized OWC prototypes have been installed and tested world widely, including Tofteshallen in Norway (500 kW), Sakata in Japan (60 kW), Pico in Portugal (400 kW), Limpet in Scotland (500 kW), and more recently Mutriku in Spain (300 kW) [9]. However, OWC technology has not been fully commercialized yet [10]. The main reason is that the hydrodynamics of the OWC devices has not been fully understood. Further hydrodynamic investigations on OWC device still need to be carried out theoretically, numerically and experimentally.

Although significant efforts have been made to investigate the hydrodynamic performance of OWC devices theoretically at the early stage, such as McCormick [11], Evans [12], Falcão and Sarmento [13], Evans [14] and Falnes and McIver [15] etc, majority of OWC theories are based on linear wave theory and neglect the viscosity, spatial variation of water surface elevation in the chamber. The hydrodynamic efficiency is generally over-predicted based on the simple theoretical solutions [8, 22, 25].

Recent development of numerical techniques and increasing computer power has significantly increased the efficiency and accuracy of numerical studies of the hydrodynamic performance of

OWC devices. Based on the potential flow model, Count and Evans [16] developed a numerical model by coupling the three-dimensional (3-D) boundary integral method outside the OWC device and with the eigenfunction expansion method in the rectangular inner region. Wang et al. [17] validated numerical computations with experimental measurements and found the topographical effects of bottom slope and water depth is important to the performance of an OWC. Delauré and Lewis [7] applied the first-order BEM to simulate the hydrodynamic performance of a 3D fixed OWC device and discussed its accuracy. Josset and Clément [18] developed a time-domain numerical model of OWC wave power plants to predict the annual performance of the wave energy plants on Pico Island, Azores, Portugal. Nunes et al. [19] analyzed an off-shore OWC device numerically and studied the techniques that could improve energy extraction efficiency. It was proved that it is possible to achieve a resonant response for sinusoidal waves with a frequency different from the device's natural frequency. Falcão et al. [20] analyzed the performance of an OWC spar buoy wave energy converter in the frequency domain for both regular and irregular waves. Iturrioz et al. [10] presented a simplified time-domain model for a fixed detached OWC device and validated numerical computations by comparison with experimental data. Gkikas and Athanassoulis [21] presented a nonlinear system identification method for modeling the pressure fluctuation inside the chamber of an OWC wave energy converter under monochromatic excitation. Ning et al. [22] developed a two-dimensional (2-D) fully nonlinear numerical wave flume (NWF) based on a time-domain higher-order boundary element method (HOBEM) and used it to investigate the hydrodynamic performance of a fixed OWC wave energy device. Rezanejad et al. [23] investigated the performance of dual chamber OWC devices in the stepped sea bottom condition.

Recently, researchers have also developed viscous-flow model based on the N-S equations to analyze the OWC device. Marjani et al. [24] simulated the flow characteristics in the chamber of an OWC system using the FLUENT software. They found that the energetic performances are higher in the case of the inhalation mode than in the case of the exhalation mode. Zhang et al. [25] developed a 2-D two-phase numerical wave tank (NWT) using a level-set immersed boundary method to study the flow field, surface elevation and air pressure in an OWC chamber. They investigated the effects of the geometric parameters on the OWC power capture efficiency. Teixeira et al. [9] applied the

Fluinco numerical model to simulate an OWC device and investigate the effects of the chamber geometry and the turbine characteristics on the device performance. López et al. [26] implemented a 2-D numerical model based on the RANS equations and the VOF surface capturing scheme (RANS-VOF) to study the optimum turbine-chamber coupling for an OWC. Luo et al. [27] developed a 2-D, fully nonlinear CFD model and analyzed the efficiency of fixed OWC-WEC devices with linear power take off systems. Iturrioz et al. [28] simulated a fixed detached OWC device using OpenFOAM to test capability of CFD simulations in analyzing the OWC device. However, it is still difficult to perfectly simulate the nonlinear wave interaction with an OWC device in any previous numerical models due to the complicated coupling process of air and water in the chamber.

In addition to the numerical modelling, a number of experiments have been carried out to study the performance of OWC devices. Tseng et al. [29] presented the concept of a breakwater and a harbor resonance chamber which can extract energy from the ocean and protect the shore at the same time. A 1/20 model of this type of system was constructed and tested in a wave tank and the experimental data were compared with the previous theoretical results. Afterward, Boccotti et al. [30] carried out an experiment to study the hydrodynamic performance of harbor resonance chambers. Morris-Thomas et al. [8] experimentally studied the energy efficiency of an OWC focused their study on the influence of front wall geometry on the OWC's performance. Gouaud et al. [31] carried out experiments to investigate the hydrodynamic performance of an OWC device and compared the experimental data to numerical results. Liu [32] studied the operating performance of an OWC air chamber both experimentally and numerically. Dizadji and Sajadian [33] carried out an experimental study on the geometrical design of an OWC system and optimized the set up for the maximizing the energy harness. He et al. [34] experimentally investigated an integrated oscillating water column type converter with floating breakwater and found that the integrated system can widen the frequency range for energy extraction. Imai et al. [35] studied the total conversion process of an OWC device with a turbine theoretically, and carried out experiment to validate the theoretical results.

Above literature review shows that a number of investigation methods have been developed and applied to study the hydrodynamic performance of the OWC device. Various numerical models have been established based on either potential-flow or viscous-flow model. However, the related experimental studies on land-fixed OWC devices are still limited, especially those on the influence of wave nonlinearity, turbine damping and bottom slope on the performance of the OWC devices. Moreover, no sufficient attention has been paid to the water motion in the chamber. The large difference between the internal and external surface elevations of the chamber can cause the dynamic pressure on the front wall, which may be a threat to the safety operation of the OWC device [36]. To complete the previous studies, the primary goal of this study is to experimentally investigate the effects of wave nonlinearity, the orifice scale and the bottom slope on the hydrodynamic efficiency of land-fixed OWC devices and the characteristics of water motion in the air chamber.

The rest of the present paper is organized as follows: The experimental procedure is described in section 2. Experimental data is compared with the solutions of the higher-order boundary element method (HOBEM) in Section 3. In Section 4, the effects of the incident wave amplitude and geometric parameters on the hydrodynamic efficiency of the OWC device are discussed. In Section 5, the spatial variation of the free surface in the air chamber is analyzed. Finally, the conclusions of this study are summarized in Section 6.

2. Experiments

2. 1 Experimental set-up

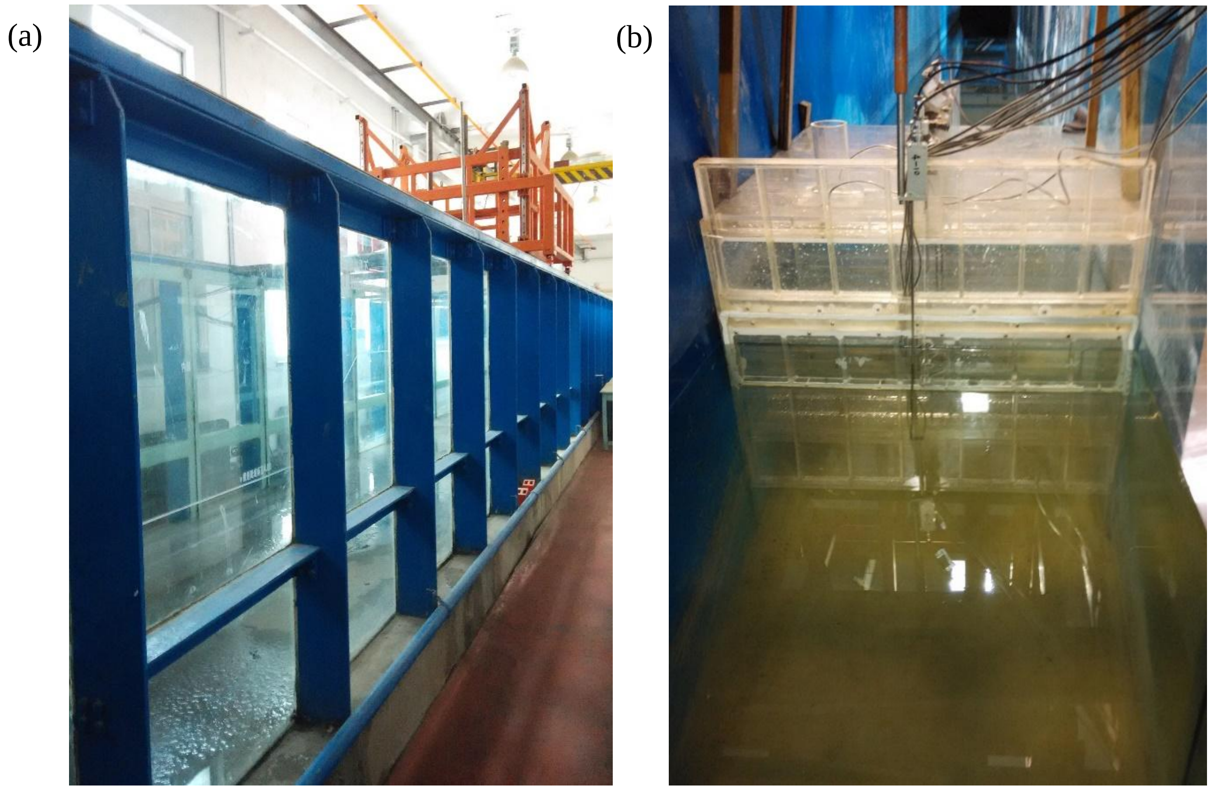

Fig. 1 Photos of (a) Laboratory wave flume and (b) OWC device.

The physical model tests were carried out in the wave-current flume at the State Key Laboratory of Coastal and Offshore Engineering, Dalian University of Technology, China. The glass-walled wave flume is 69 m long, 2 m wide and 1.8 m deep as shown in Fig. 1 (a). The piston-type wave maker is installed at one end of the flume, and a wave-absorbing beach is located at the other end to absorb the outgoing waves. The wave maker is able to generate regular and irregular waves with periods from 0.5 s to 5.0 s. The test section of the flume was divided into two parts along the longitudinal direction, which were measured as 1.2 m and 0.8 m in width, respectively. The OWC model was installed in the 0.8 m wide part and 50 m away from the wave maker (see Fig. 2 (b)). To avoid wave energy transfer through the device, the model was designed to span across the width and depth of the flume. The main body of the model was made of 8-mm thick transparent Perspex sheets, in order to have a clear view of the internal free-surface of the water.

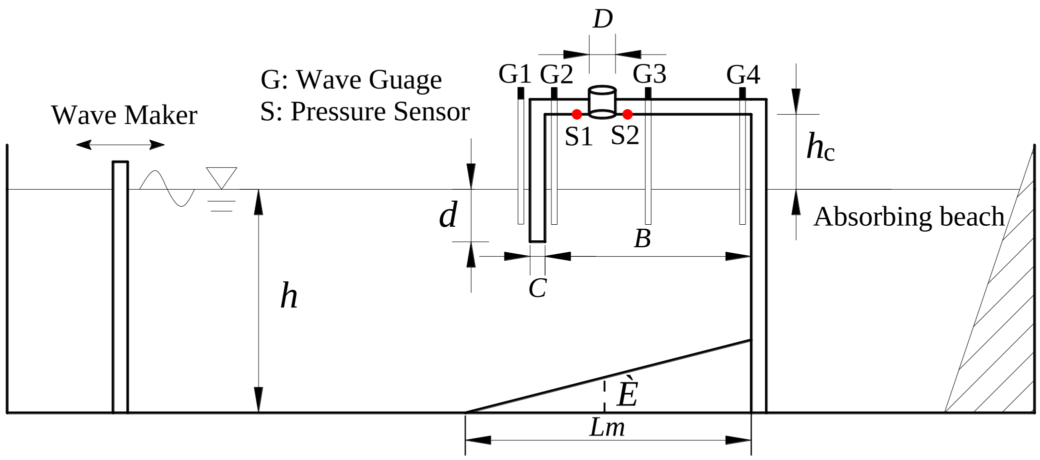

(a) Side view

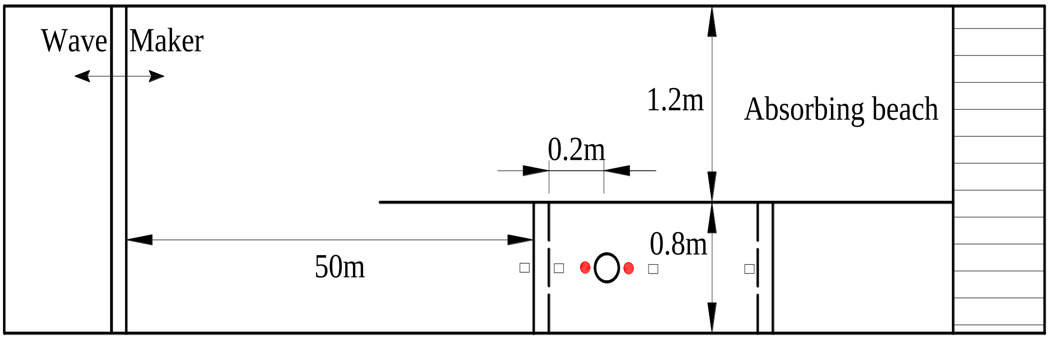

(b) Plan view

Fig. 2 Schematic of the experimental setup.

The power take-off was implemented through a circular orifice situated on the roof of the chamber and 0.2 m from the front wall (see Fig. 2). The sketch of the experimental setup is shown in Fig. 2, in which h denotes the static water depth, B the chamber width, C the thickness of the front wall, D the diameter of the orifice, d the immergence of the front wall, L_m the base length of the sea bottom slope, θ the slope angle of the bottom, and h_c the height of the air chamber (i.e., distance between the still water surface and the ceiling). In the experiments, four resistance-type wave gauges (G1, G2, G3, G4) with resolution of 0.01 cm were used to measure the instantaneous surface elevations at different locations. One exterior wave gauges was situated 0.02 m from the outer side of the front wall to measure and record the time series of free-surface wave elevation outside the chamber. Three were situated inside the OWC chamber, in which one was 0.02 m from the inner side of the front wall, the second one was at the mid-point of the chamber and the last one was 0.02 m from the rear wall. Two pressure sensors (S1 and S2) were used to measure the air pressure inside the chamber, which were placed rigidly 0.02 m from the edge of the orifice (see Fig. 2). Their average value is regarded as the air pressure in the chamber. Both the surface and pressure signals are sampled at 50 Hz. A high-speed CCD camera was used to record the whole water surface motion in the chamber with a frame rate of 100 fps.

Five sets of experiments were carried out to investigate the effects of the incident wave amplitude, chamber width, front wall draught, orifice diameter and bottom slope on the hydrodynamic performance of the OWC. The front wall thickness C=0.04 m and the chamber height h_c=0.20 m were remained constant in the experiments. Parameters B=0.55 m, d=0.14m, θ=0°, and D=0.06 m were chosen as the references. Then only one corresponding parameter would be varied in each set of experiment and the others were kept constant. The geometric parameters chosen for the experiment are shown in Table 1.

Table1 Geometric parameters used in the experiments

B(m)	d (m)	θ (°)	C (m)	D (m)	h_c(m)	L_m(m)
0.55	0.14	0	0.04	0.04	0.2	1.0
0.70	0.17	10	0.04	0.06	0.2	1.0
0.85	0.20	20	0.04	0.08	0.2	1.0
-	-	30	0.04	-	0.2	1.0

By keeping the still water depth constant at h=0.8 m, different wave conditions with wave amplitudes A_i varied in the range of (0.02 m, 0.07 m) and 14 wave periods T in the range of (0.95 s, 2.35 s) were considered. In the cases for the effects of the geometric parameters on the OWC efficiency, the incident wave amplitude was fixed at A_i=0.03 m. Total 177 tests were carried out to study the hydrodynamic performance of the OWC device.

2. 2 Data analysis

Influenced by the incident waves, the water surface in the chamber is not flat and the water column may experience both sloshing and piston motions, which influence the natural frequency of the OWC system. The mean power absorbed by the OWC device depends primarily on the heave motion of the water column and air pressure inside the air chamber. Brendmo et al. [37] reported that when wavelength is long enough in comparison with the characteristic horizontal dimension of the inner

OWC surface, surface motion at one point can represent the whole surface variation in the chamber. In the present paper, the horizontal dimension of the interior chamber of the OWC is small when compared with the prevailing wavelength. The water surface motion at the mid-point (G3) is used to represent the internal surface fluctuation for calculating the hydrodynamic efficiency.

The hydrodynamic efficiency of an OWC device is determined as [8]

$$\xi = \frac{P_0}{P_\mathrm{w} w}, \tag{1}$$

where P_w is the time-average energy flux of the incident waves, w is the width of the flume section used and P_0 is the hydrodynamic energy absorbed from the waves by the OWC device during one wave period, which is calculated by

$$P_0 = \int_{S_\mathrm{f}} \overline{p(t)\cdot u(t)}\, dt = \frac{Bw}{T}\int_t^{t+T} p(t)\cdot u(t) dt, \tag{2}$$

where $p(t)$ is the air pressure in the chamber, $u(t)$ is the normal vertical velocity of interior free surface (represented by the surface at the chamber center), S_f is the cross-section area of the free surface in the chamber and B is the width of the chamber.

According to linear wave theory, the average energy flux per unit width in the incident wave is given by

$$P_\mathrm{w} = \frac{1}{2}\rho g A_\mathrm{i}^2 c_g, \tag{3}$$

where ρ is the water density, g is the gravitational acceleration, A_i is the incident wave amplitude and c_g is the group velocity of the incident wave defined as

$$c_g = \frac{c}{2}\left(1 + \frac{2kh}{\sinh 2kh}\right), \tag{4}$$

where k is the wave number; c is the incident wave velocity

$$c = \frac{\omega}{k}, \tag{5}$$

and the angular frequency ω satisfies the following dispersion relation

$$\omega^2 = gk \tanh kh. \tag{6}$$

3. Comparisons between experimental data and numerical results

A two-dimensional fully nonlinear numerical model based on the potential theory and the time-domain HOBEM by Ning et al. [22] is used to simulate the proposed hydrodynamic performance of an OWC device and the numerical results are compared with the experimental data. In the numerical model study, the incident wave is generated by the inner-domain sources whose strength is dependent on the incident wave velocity. A damping layer with a coefficient $\mu_1(x)$ at the inlet of the numerical flume is implemented to absorb the reflected wave from the OWC device as shown in Fig. 3. The reflected waves from the structure can pass through inner-domain sources (i.e., the incident surface) and then absorbed at the inlet damping layer with nearly none re-reflection. The relative study is given in the Appendix A detailedly. The governing equation is changed from Laplace equation to Poisson equation. To model the viscous effect due to water viscosity and flow separation in the potential flow model, the linear damping term can be used in the free surface boundary of a sloshing container [38] or a narrow gap between twin floating objects [39, 40]. In the study [22], an artificial viscous damping term with a coefficient μ_2 is applied to the dynamic free surface boundary condition inside the OWC chamber. Then, velocity potential also satisfies the following modified fully nonlinear free surface boundary conditions

$$\begin{cases} \dfrac{dX\left(x,z\right)}{dt} = \nabla\phi - \mu_1\left(x\right)\left(X - X_0\right) \\ \dfrac{d\phi}{dt} = -g\eta + \dfrac{1}{2}\left|\nabla\phi\right|^2 - \dfrac{p}{\rho} - \mu_1\left(x\right)\phi - \mu_2\dfrac{\partial\phi}{\partial n} \end{cases}, \tag{7}$$

where X_0=(x_0, 0) denotes the initial static position of the fluid particle. The damping coefficient $\mu_1(x)$ is defined by

$$\mu_1\left(x\right) = \begin{cases} \omega\left(\dfrac{x - x_1}{L}\right)^2, & x_1 - L < x < x_1 \\ 0, & x \geq x_1 \end{cases}, \tag{8}$$

where x_1 is the starting position of damping zone, L is the length of the damping zone at the left flume-end and equals to one incident wavelength in the present study. The artificial viscous damping coefficient μ_2 is determined by trial and error (the detailed determination process is shown in

Appendix B) and only implemented inside the chamber.

The air pressure p on the water free surface is set to be zero (i.e., atmospheric pressure) outside of the chamber. Inside the chamber, the pneumatic pressure is given by

$$p(t) = C_{\mathrm{dm}} U_{\mathrm{d}}(t), \tag{9}$$

where C_{dm} is linear pneumatic damping coefficient and U_{d}(t) the air flow velocity in the orifice.

The energy absorbed by the OWC device in the numerical model can be calculated by

$$P_0 = \frac{1}{T}\int_t^{t+T} Q(t)p(t)\,dt = \frac{1}{T}\int_t^{t+T} B\bar{\dot{\eta}}(t)p(t)\,dt = \frac{1}{T}\int_t^{t+T} C_{\mathrm{dm}} U_{\mathrm{d}}(t) A U_d(t)\,dt, \tag{10}$$

where the flow rate $Q(t)=B\bar{\dot{\eta}}(t)=AU_{\mathrm{d}}(t)$. $\bar{\dot{\eta}}(t)$ is the time mean vertical velocity of the free surface inside the chamber. More details regarding the numerical model can be found in [22].

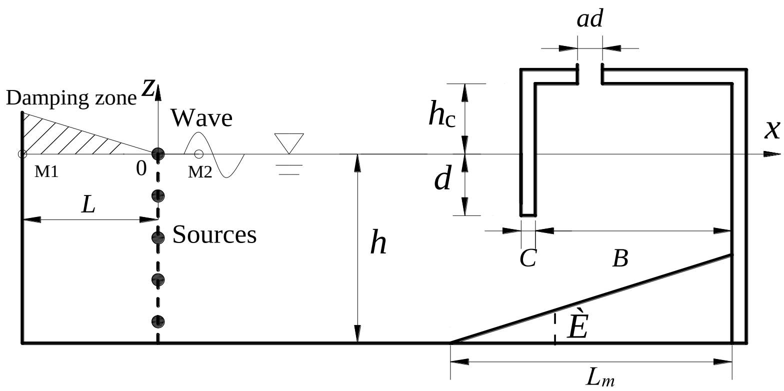

Fig. 3 Sketch of the numerical wave flume.

The numerical results with the parameters: chamber width B=0.55 m, front wall thickness C=0.04 m, front wall draught d=0.14 m, bottom slope θ=0° and the orifice diameter D=0.06 m, are compared with the experimental data. In the numerical model, the air duct width ad is set as 0.0036 m, which is of the same area with the circular air orifice in the experiment, and the other four parameters are the same as those used in the experiment. The incident wave amplitude is A_{i}=0.03 m. The viscous coefficient and the linear pneumatic damping coefficient in Eqs. (7) and (9) are set as μ_2=0.2 and C_{dm}=9.5, respectively. The length of the numerical flume is set to 5λ, in which 1.0λ at the left side is used as the damping layer. And the size of the boundary elements in the horizontal direction is $\Delta x=\lambda/30$. For each case, 30 periods of waves are simulated with a time step of $\Delta t=T/80$.

Figs. 4 (a) and (b) show the time series of the surface elevation at the chamber center for T=1.366 s and T=1.610 s, respectively. Overall, the measured and predicted surface elevation compare well with each other. However, the numerical model did not capture the secondary harmonic peaks observed in the experiment in Fig. 4 (a). This is likely due to the fact that the present pneumatic model is linear, therefore, is unable to predict the higher harmonics generated by the interaction between the high frequency wave and the inhaled air flow. To verify this point, Figs. 5 (a) and (b) show the surface elevation spectrums at points outside the chamber (G1) and inside the chamber (G3) for T=1.366 s. Fig. 5 (a) indicates good agreement between the numerical model and experiment at G1 outside the chamber, where the highest harmonic energy occurs at the second harmonic frequency without the pneumatic influence in the chamber. However, the highest harmonic energy occurs at the fourth harmonic frequency as observed at G3 by experiment in Fig. 5 (b), which is due to the pneumatic effect by comparison with the result in Fig. 5 (a) and are not resolved by the present linear pneumatic model. Figs. 6 (a) and (b) presents the time series of air pressure in the chamber for T=1.366 s and T=1.610 s, respectively. Better agreements between the observed and predicted results are obtained.

Fig. 7 gives the variation of the hydrodynamic efficiency with the dimensionless wave number kh. The comparisons between the experimental data and the potential numerical results with μ_2=0.0 (i.e., no considering the viscous effects) and μ_2=0.2 (i.e., considering the viscous effects) are shown in the figure. It can be seen that the pure potential solutions (i.e., μ_2=0.0) over-predict the hydrodynamic efficiency because it neglects the viscous damping, but the resonant frequencies predicted by the potential model with and without the damping term agree well with each other. The viscous effect on the hydrodynamic efficiency is more obvious in the resonant zone (i.e., $1.2<kh<2.2$) than at the other wave number ranges. In addition, the shape of the calculated hydrodynamic efficiency curves are similar to each other. Overall, the potential model results with a certain damping term agree well with the experimental data. It is also noted that there are two experimental data lying in between the two potential results near kh=2.5, which may be due to the experimental error or a larger damping coefficient μ_2 defined. Furthermore, it can be seen that both the numerical results with the viscous term and experimental data indicate that the optimal point is around kh=1.58 with the hydrodynamic efficiency of 0.83 for this geometry.

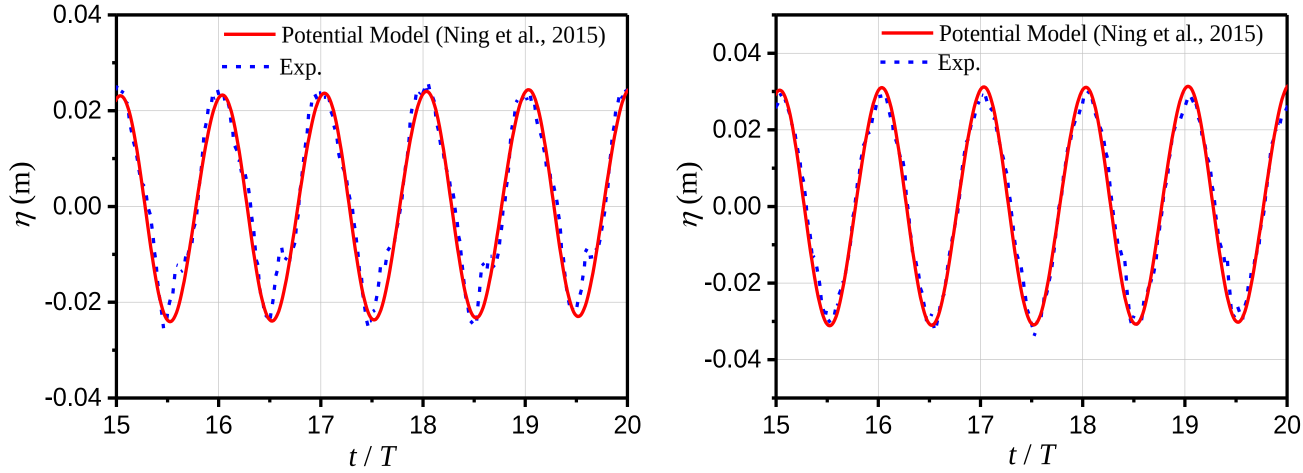

(a) T=1.366 s (b) T=1.610 s

Fig. 4 Time series of the predicted (solid line) and observed (dashed line) surface elevation at the chamber center at T=1.366 s and 1.610 s

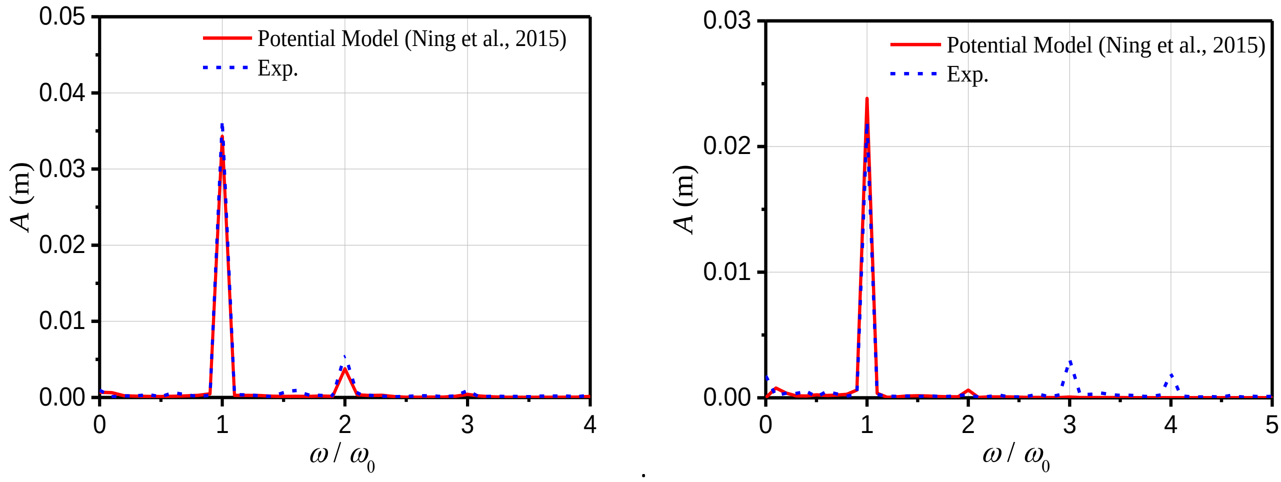

(a) at G1 (b) at G3

Fig. 5 Spectrum analysis of surface elevations at outside the chamber (G1) and chamber center G3 for T=1.366 s

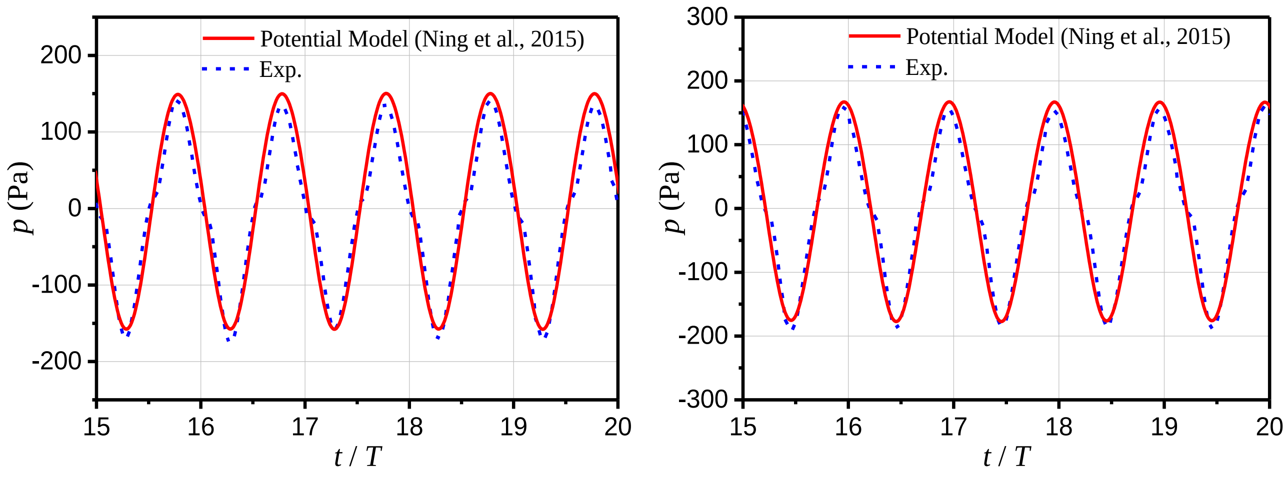

(a) T=1.366 s (b) T=1.610 s

Fig. 6 Time series of the predicted (solid line) and observed (dashed line) air pressure in the chamber at T=1.366 s and 1.610 s.

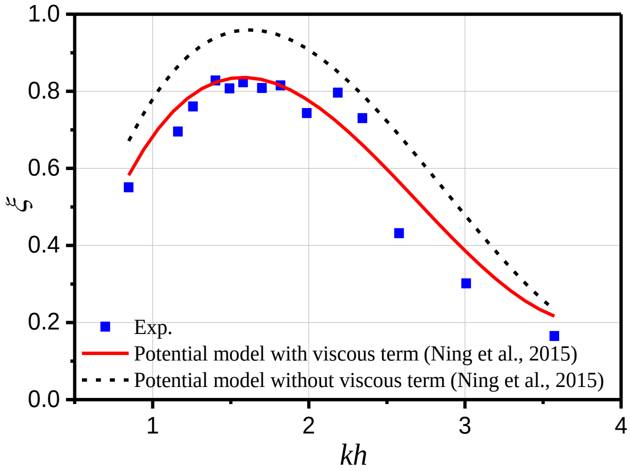

Fig. 7 Variation of the predicted and observed hydrodynamic efficiency with *kh*.

4. Effects of wave and geometric parameters

The influences of the incident wave amplitude (i.e., wave nonlinearity) and the OWC geometric parameters including the chamber width, the front wall draught, the orifice scale and the bottom slope on the hydrodynamic efficiency are examined in this section. Both the experimental data and their cubic fitting curves are included in the relevant figures. The similar fitting method can be found in Zhang et al. [25].

4. 1 Incident wave amplitude

To investigate the effect of the wave nonlinearity on the hydrodynamic efficiency of the OWC device, the experiments were carried out with different incident wave amplitudes and constant other parameters: B=0.55 m, d=0.14 m, D=0.06 m and θ=0°. Fig. 8 shows the variation of the hydrodynamic efficiency with kh for the incident wave amplitudes A_i =0.02 m, 0.03 m and 0.04 m. It can be seen that wave amplitude has little influence on the resonant frequency and the efficiency curve shape. While the resonant frequencies for all the three wave amplitudes occur at kh=1.58, the hydrodynamic efficiencies for A_i =0.02 m, 0.03 m and 0.04 m are of 0.81, 0.83 and 0.78, respectively. In addition, it can be observed that the overall hydrodynamic efficiency increases as the wave amplitude A_i increases from 0.02 m to 0.03 m, and decrease as A_i increases from 0.03 m to 0.04 m. The maximum efficiency is at A_i =0.03 m among these three wave amplitudes.

To further illustrate the relationship between the wave nonlinearity and the hydrodynamic efficiency, Fig. 9 shows the variation of the hydrodynamic efficiency with the incident wave amplitude at three frequencies of *kh*=1.40, 1.58 and 1.82. It can be observed that the hydrodynamic efficiency firstly increases with increasing wave amplitude, and reaches the maximum at a critical A_i, then decreases as wave amplitude further increases. Such behavior is in agreement with the numerical results presented by Ning et al. [22]. When studying OWC in irregular waves, López et al. [41] also observed that the capture factor increases with the wave steepness at low wave frequencies and decreases at high wave frequencies. But the critical wave amplitude A_i corresponding to the peak efficiency was not presented in their work. In addition, the peak efficiency at the resonant frequency (i.e., *kh*=1.58) decreases more quickly with increasing amplitude than those at *kh*=1.40 and *kh*=1.82.

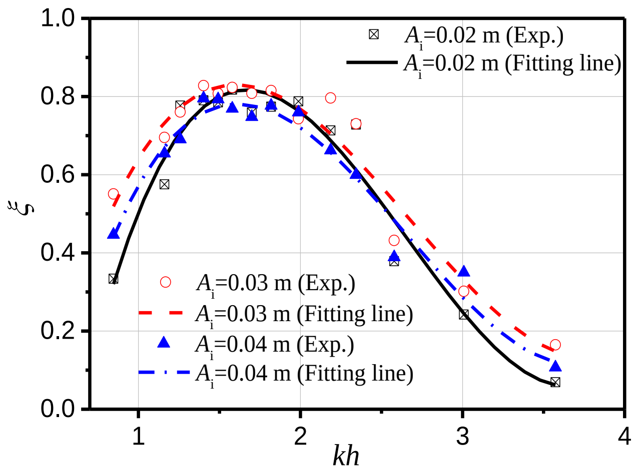

Fig. 8 Hydrodynamic efficiency versus dimensionless wave number for A_i=0.02 m, 0.03 m and 0.04 m.

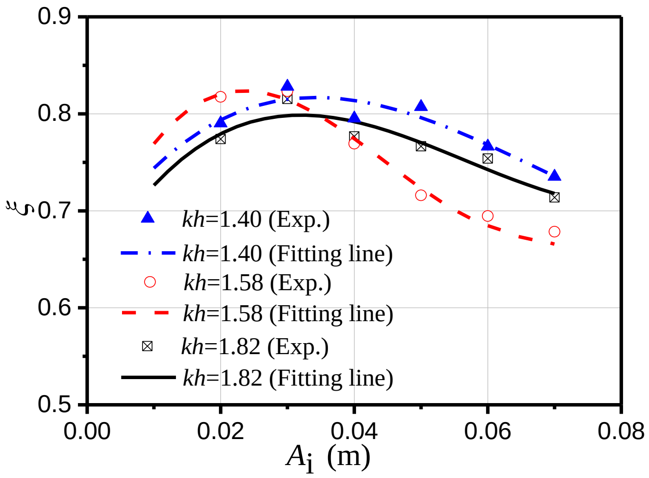

Fig. 9 Hydrodynamic efficiency versus incident amplitude A_i for *kh*=1.40, 1.58 (resonant frequency) and 1.82.

4. 2 Chamber width

Fig. 10 shows the hydrodynamic efficiency of the OWC device for three different chamber widths: *B*= 0.55 m, 0.70 m and 0.85 m and constant wave amplitude of A_i=0.03 m. The other parameters are kept the same as those in Fig. 8. From the figure, it can be seen that the chamber width has a significant influence on the hydrodynamic efficiency of the OWC device. The hydrodynamic efficiency increases with the increase of chamber width *B* in the low-frequency region (about *kh*<1.5), but follows a completely opposite trend in the high-frequency region. What's more, the resonant frequency decreases with the increase of *B*. The optimal points are around *kh*=1.58 (*B*=0.55

m), *kh*=1.50 (*B*=0.70 m) and *kh*=1.36 (*B*=0.85 m) with the same hydrodynamic efficiency of 0.83, respectively. The reason is due to that the inertia of the OWC water column increases with chamber width. The approximated nature piston frequency formula by Veer and Thorlen [42] for the water mass oscillating in a moonpool is calculated as follows:

$$\omega_n = \sqrt{\frac{g}{d + 0.41\sqrt{Bw}}}. \tag{11}$$

The coefficient 0.41 in the above formula is empirical and hence does not necessarily provide accurate results in the case of OWC device. However, the dependence of the natural frequency on the width of the chamber can be clearly seen in Eq. (11).

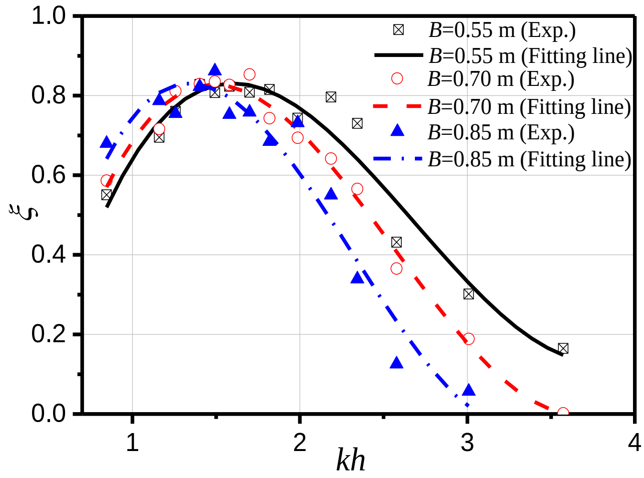

Fig. 10 Hydrodynamic efficiency versus dimensionless wave number for different chamber widths

4. 3 Front wall draught

Fig. 11 illustrates the hydrodynamic efficiency of the OWC device obtained from different front wall draughts of *d*=0.14 m, 0.17 m and 0.20 m with A_i=0.03 m and other parameters remaining the same as those in Fig. 8. Firstly, it can be observed that both the resonant frequency and the peak efficiency decrease with the increase of the submerged depth *d*. They occur at *kh*=1.59 (*d*=0.14 m), 1.50 (*d*=0.17 m) and 1.41 (*d*=0.20 m) corresponding to the hydrodynamic efficiency of 0.83, 0.77 and 0.76, respectively. This characteristic is caused by the increased mass of water column in the chamber. The hydrodynamic efficiency reduces significantly with increasing *d* in the high-frequency zone (about *kh*>1.75) and is not sensitive to the change of draught *d* in the low-frequency zone (about *kh*<1.0). An explanation to such a phenomenon is that while in the low-frequency long wave region, compared with the wave length, the draught of the front wall is small enough, so that the variation of the long wave length is insensitive to the submerged depth. In contrast, in the high-frequency short wave region, the draught of the front wall is not small relative to the wavelength, so the variation of the short wave length is sensitive to the immergence depth [22].

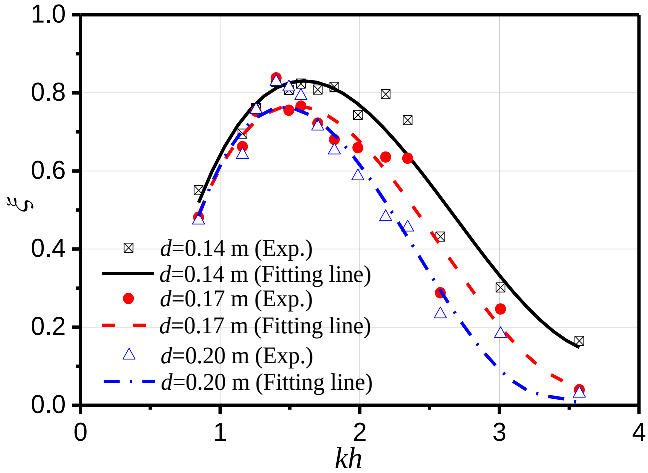

Fig. 11 Hydrodynamic efficiency versus dimensionless wave number *kh* for different draught *d*

4. 4 Orifice scale

As shown in Fig. 12, three circular-shaped openings were tested in the experiments. The size of an opening can be described by the opening area ratio $\varepsilon = S_0/S$, where S_0 and S are the cross-sectional areas of the orifice and the air chamber, respectively. In this set of experiments, the incident wave amplitude was set as A_i=0.03 m and other parameters were kept the same as those in Fig. 8. Three diameters of the orifice D=0.04 m, 0.06 m and 0.08 m correspond to the opening ratios of 0.29%, 0.66% and 1.17%, respectively. The optimal hydrodynamic efficiency ξ is highly influenced by the opening ratio with ξ=0.63 (ε=0.29%), 0.83 (ε=0.66%) and 0.74 (ε=1.17%). Moreover, the hydrodynamic efficiency ξ for ε=0.66% reaches the largest among the three opening ratios except those in the high-frequency zone (about kh>2.6). He and Huang [43] obtained a similar conclusion in their experimental study of pile-supported OWC-type structure. They found that the circular-shaped opening with an opening ratio of 0.625% could achieve the smallest transmission coefficient. To further explain such phenomenon, Figs. 13 and 14 present the comparisons of the air pressure in the chamber and the maximum water surface elevation at the chamber center for different opening ratios, respectively. The water column motion is influenced by the oscillation of the air pressure inside the chamber. Experimental results show that internal air pressure decreases with increasing opening ratio, while the maximum surface elevation changes with an opposite trend. For the smallest opening ratio ε=0.29% (i.e., D=0.04 m), the largest pressure fluctuation in the chamber leads to the smallest oscillation amplitude of the water column. For the largest opening ratio ε=1.17% (i.e., D=0.08 m), the pressure fluctuation in the chamber is the smallest with the largest surface elevation. The wave energy extraction attributes to the product of air pressure and volume variation in the chamber according to Eq. (2). Thus the optimal ones correspond to the opening ratio ε=0.66% (i.e., D=0.06 m) from Figs. 12, 13 and 14. The present analysis may help to determine the turbine damping of the OWC device to achieve the optimal energy extraction.

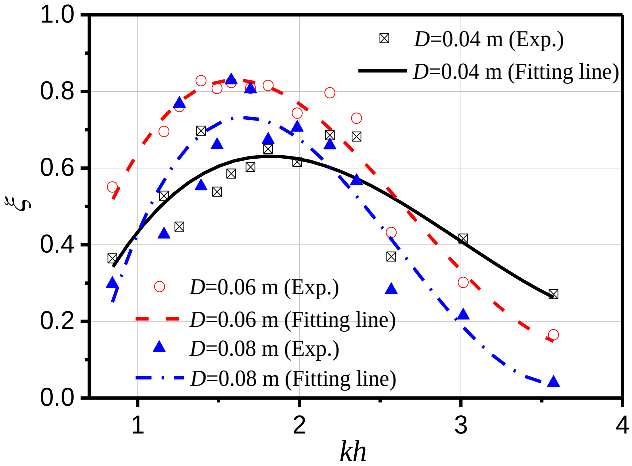

Fig. 12 Variation of hydrodynamic efficiency for different diameter of the air orifice D= 0.04 m (open ratio ε=0.29%), 0.06 m (open ratio ε=0.66%) and 0.08 m (open ratio ε=1.17%).

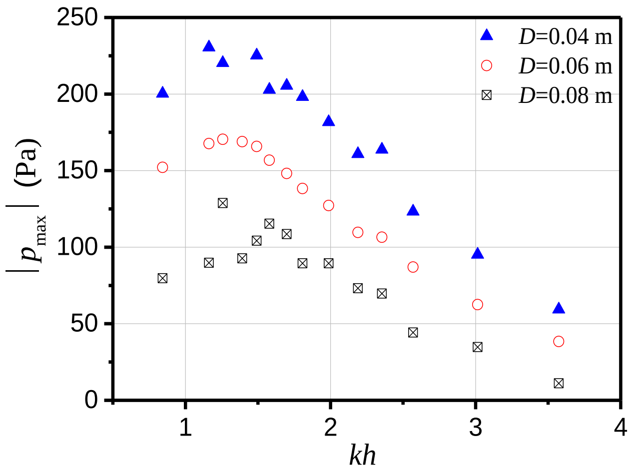

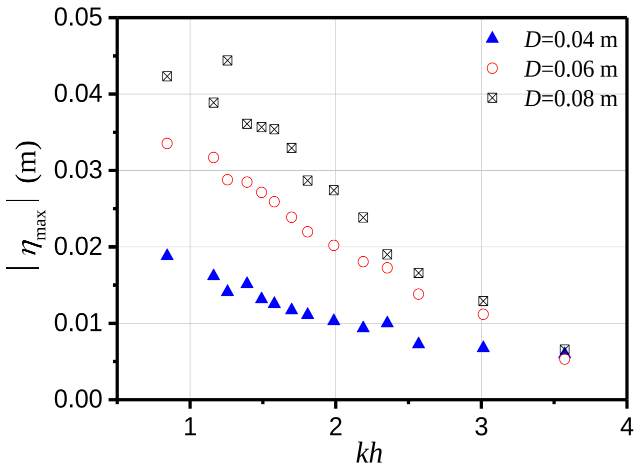

Fig. 13 Variation of the air pressure in the chamber for different diameter of the air orifice.

Fig. 14 Variation of the surface elevation at the chamber center for different diameter of the air orifice.

4. 5 Bottom slope

To investigate the influence of the bottom slope on the performance of the OWC device, physical tests are carried out for different bottom slopes with the parameters A_i=0.03 m, B=0.55 m, d=0.14 m, D=0.06 m and L_m=1.0m being constant. As shown in Fig. 15, the results indicate that the efficiency curve is shifted slightly to the left with the increase of the slope angle θ. The resonant frequency is basically unchanged and occurs at about kh=1.58. Rezanejad et al. [23] reported that the efficiency curve slightly shifts to the lower wave period with the decrease of the bottom slope in the case without stepped bottom in their study of the dual-chamber OWC. Ashlin et al. [44] experimentally studied the performance of an OWC device with different bottom profiles subject to random waves and found that the nature frequency is independent of the bottom profile.

Fig. 16 shows the variation of the hydrodynamic efficiency versus bottom slope for different kh. The largest efficiency occurs at the resonant frequency (i.e., kh=1.58) and slightly increases with the bottom slope in the proposed scope of $\theta \leq 30$ degree. This attributes to the largest product of the surface variation rate $\left(\eta_{\max}\text{-}\eta_{\min}\right)/T$ and air pressure variation rate $\left(p_{\max}\text{-}p_{\min}\right)/T$ in the chamber at resonant frequency (see Figs. 17 (a) and (b)). For the low-frequency (kh=1.26), the hydrodynamic efficiency increases with increasing slope angle. This is because the water depth in the chamber decreases with increasing slope angle, which can enhance the shallow water effect and strengthen the piston motion in the chamber. For the high-frequency (kh=1.99), the increase of the slope angle can lead to a stronger reflection from the sloping bottom for the short waves with a weak transmission capability. Thus, the hydrodynamic efficiency decreases with increasing slope angle.

From Fig. 17, it can be seen that the difference in between surface variation rates for different kh is small for some special bottom slopes. The result indicates that a proper bottom slope can provide a work space in the OWC chamber almost independent on the sea wave conditions. This is important for the structure safety and operation stability. Because the real sea bottom is not plan, this will provide a good reference to explore a proper site for the OWC wave energy converter to be constructed.

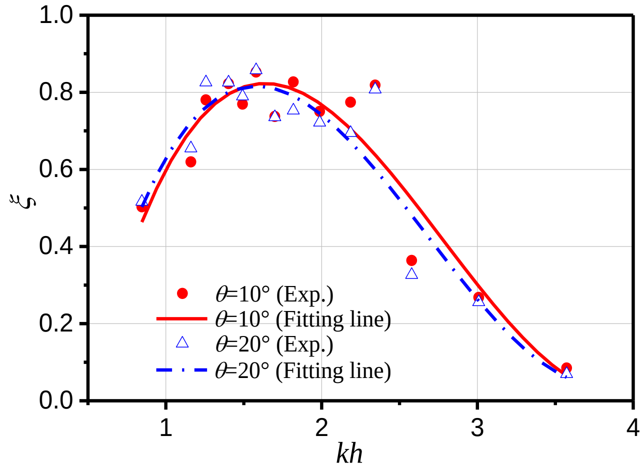

Fig. 15 Variation of the hydrodynamic efficiency for different bottom slope θ.

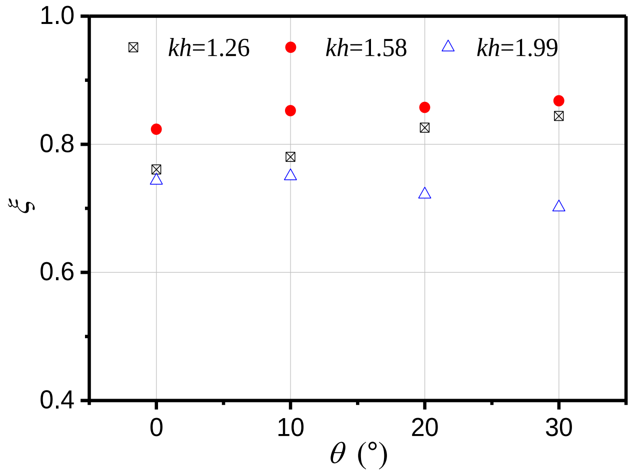

Fig. 16 Variation of the hydrodynamic efficiency versus θ for different kh=1.26, 1.58 (resonant frequency) and 1.99.

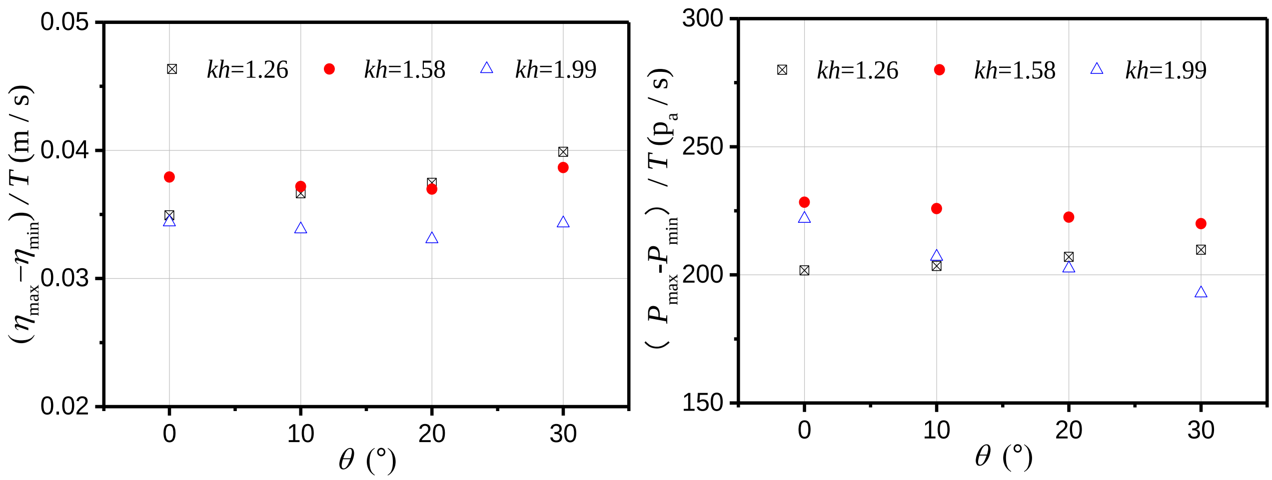

(a) Free surface variation rate (b) Air pressure variation rate

Fig. 17 Variation of the free surface and air pressure rate in the chamber versus θ for different kh=1.26, 1.58 (resonant frequency) and 1.99.

5. Water motion outside and inside the chamber

To investigate the spatial variation of the free surface, four wave gauges were used to measure the wave elevations at locations as described in Fig. 2. The free surface motion in the chamber is quite complicated and strongly influenced by the chamber geometry and the incident wave conditions. The following parameters, including wave amplitude A_i=0.03 m, chamber width B=0.70 m, front wall draught d=0.14 m, orifice diameter D=0.06 m and bottom slope angle θ=0°, are chosen in this section.

Fig. 18 shows the relative maximum surface amplitude $|\eta_{max}|/A_i$ at each gauging point versus the dimensionless wave length λ/B. It can be seen that the three maximum surface amplitudes inside the chamber increase with the increase of wave length, while the surface amplitude outside the chamber presents an opposite trend. This is because that the long wave possesses a strong transmission capability and a large part of the wave energy is transmitted into the chamber. The maximum surface amplitudes at G2 and G4 reach the largest at λ/B=2 (i.e., T=0.950, λ=1.40 and B=0.70), but the relating surface amplitude at chamber center, i.e., G3, is near to zero. This is due to the so called seiching phenomenon excited when λ/B=2. A similar phenomenon was ever reported by Liu et al. [45] numerically.

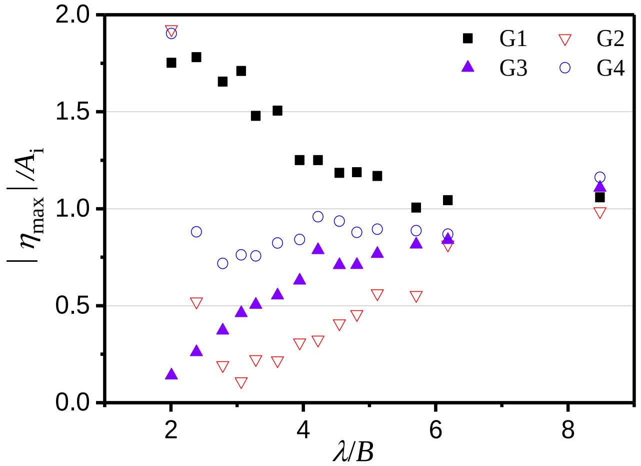

Fig. 18 Variation of the relative maximum surface amplitude with the dimensionless wave length at four gauges.

Fig. 19 (a) and Fig. 20 (a) may help to further explain this special seiching phenomenon. Fig. 19 (a) shows the time series of the surface elevation at the gauges with a wave period T=0.950 s

(λ/B=2.01). It is found that, there is a phase difference of half period (i.e., $T/2$) between G2 and G4, and the amplitudes at G2 and G4 are nearly twice the incident wave amplitude. However, the surface elevation at G3 has a very weak fluctuation and its mean value is below the still water surface. This is because of the pneumatic pressure resulting in the lower mean surface in the chamber. Fig. 20 (a) shows the snapshot of surface elevation in the chamber with T=0.950 s. It can be seen that, the water surface in the chamber is rising at one wall and falling at the other wall and the intersection node of two lines lies at the chamber center. This is the typical standing wave characteristics. Furthermore, the total mass inside the chamber is not changed [45] and the air pressure is also kept constant which is close to the atmospheric pressure. Thus, no energy can be extracted from the waves, which can be seen the dashed line for case of B=0.70 m in Fig. 10 (i.e., the hydrodynamic efficiency is near to zero for kh=3.57 corresponding to T=0.950s and λ/B=2.01). Therefore, such seiching phenomenon should be avoided in the OWC design.

In addition, from Fig. 19 (b), (c) and (d), it can be seen that the phase difference between the G1 and G2 decreases with the increase of wave length. That is to say, the long wave generates more synchronized surface motion inside and outside the chamber than the short wave. This is benefit to the safety of the OWC device to avoid the large wave pressure on the front wall caused by the apparent phase difference between the internal and external surface elevation of the chamber.

Overall, it is evident from Figs. 18, 19 and 20 that the surface elevation at the three observed points inside the chamber become closer to each other with the increase of wave length. It means that the interior water surface tends to a horizontal line, which proves that it is feasible to use a point to represent the water column motion inside the chamber for long waves in Eq. (2). From Fig. 7, it can also be seen that there is good match between the measured efficiency and the improved potential solution for long waves in the low-frequency zone. However, due to the spatial variation of surface elevation in the chamber, there exists the apparent discrepancy between them for short waves in the high-frequency zone. It means that there may be some errors in calculating the experimental hydrodynamic efficiency by using the chamber center to represent the average motion of the water column in the chamber for some short waves.

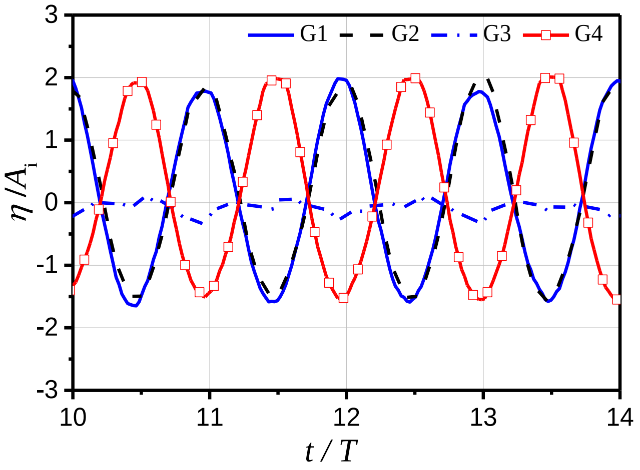

(a) T=0.950 s, λ/B=2.01

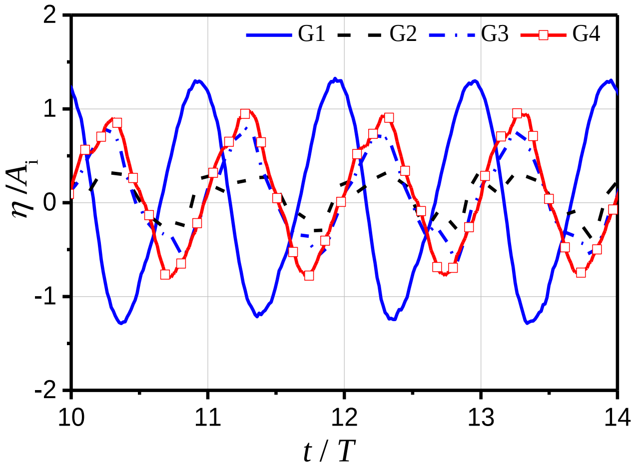

(b) T=1.366 s, λ/B=3.95

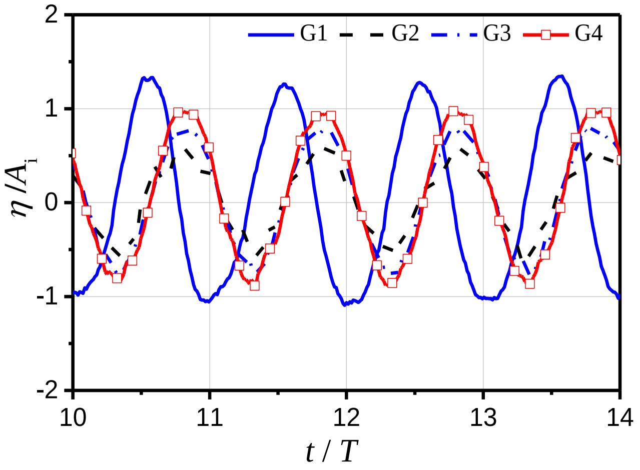

(c) T=1.610 s, λ/B=5.12

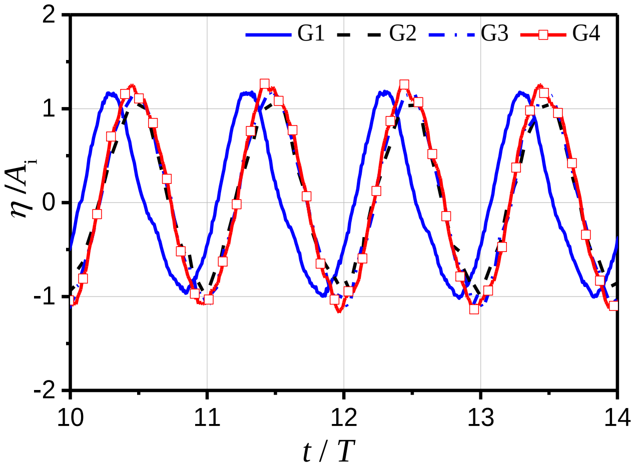

(d) T=2.350 s, λ/B=8.48

Fig. 19 Time series of surface elevations at four wave gauges for A_i=0.03 m, B=0.70 m, d=0.14 m, D=0.06 m and θ=0°.

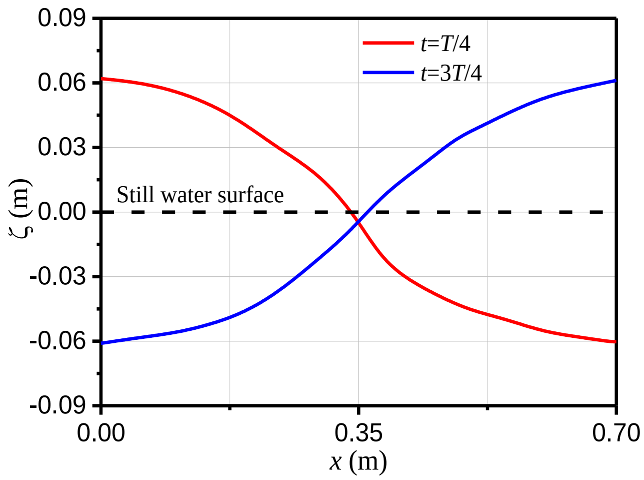

(a) T=0.950 s, λ/B=2.01

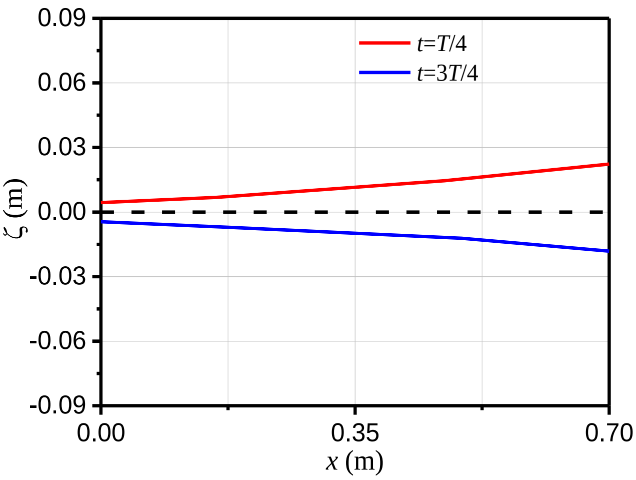

(b) T=1.366 s, λ/B=3.95

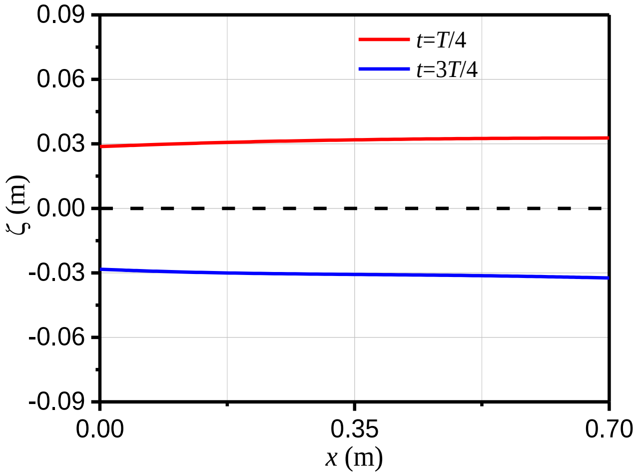

(c) T=2.350 s, λ/B=8.48

Fig. 20 Snapshots of surface elevations profiles in the chamber taken by CCD camera for wave periods T=0.950 s, 1.366 s and 2.350 s.

6. Conclusions

In the present work, the hydrodynamic performance of a fixed OWC Wave Energy Converter is experimentally investigated. The effects of the incident wave amplitude and geometric parameters on the hydrodynamic efficiency and water motion inside and outside the chamber were examined. The measured surface elevation at the chamber center, the air pressure in the chamber and the hydrodynamic efficiency agree well with the improved potential numerical model.

The incident wave amplitude has little influence on the resonant frequency and the hydrodynamic efficiency. However, the hydrodynamic efficiency increases firstly to a peak value and then decreases with the increase of the incident wave amplitude. The hydrodynamic efficiency decreases rapidly after the peak value with increasing the incident wave amplitude at the resonant frequency. With increasing the chamber width B, the hydrodynamic efficiency increases in the low-frequency region, and it follows a completely opposite trend in the high-frequency region. Meanwhile, a lower resonant frequency occurs due to the greater water mass in the chamber for a larger width B. Larger submerged depth d leads to a lower hydrodynamic efficiency ξ and a lower resonant frequency. The opening ratio has a significant influence on the peak value of the hydrodynamic efficiency. The present results show that the optimal hydrodynamic efficiency occurs at the opening ratio ε=0.66%. In the range of $\theta \leq 30°$, the bottom slope has little influences on the resonant frequency, but the optimal efficiency increases with the increase of bottom slope. A proper bottom slope can provide a work space in the OWC chamber almost independent on the sea wave conditions.

The water surface motion in the chamber is highly dependent on the relative wave length λ/B. Seiching phenomenon, which leads to no energy extracted from the waves, can be excited when the relative wave length is λ/B=2. This phenomenon should be avoided in the design of an OWC device. With the increases of the relative wave length (λ/B >2), the mode of sloshing motion decreases and the mode of piston motion increases. Meanwhile, the phase difference of free surface between the inside and outside the chamber also decreases.

The present investigation can be a guideline to assist in the geometry optimization design, site selection, and safety analysis of the land-based OWC devices and provide experimental data for validating numerical models.

Acknowledgements

The authors also would like to gratefully acknowledge financial support from the National Natural Science Foundation of China (Grant Nos. 51179028, 51222902, 51490672), the Program for New Century Excellent Talents in University (Grant No. NCET-13-0076) and the Joint Project between NSFC and RS (Grant No. 51411130127).

Appendix A: Absorption ability of the damping layer

The absorption ability of the damping layer was tested in a case with the following parameters A_i=0.03 m, T=1.610 s, B=0.55 m, D=0.06 m, d=0.14 m and θ=0°. Fig. A1 shows the time series of surface elevations at two different positions (i.e., M1 and M2) as marked in Fig. 3. M1 is at the left flume-end (i.e., the ending position of the damping layer, x= -L) and M2 is at x=0.5L. It can be seen that the relative wave amplitude at the left flume-end (M1) is less than 0.03, which means that most of reflected wave energy was absorbed in the damping layer. Fig. A2 shows the relative wave height ($H/2A_i$) distribution along the damping layer. The wave height attenuates rapidly to a very small value (less than 3% of the incident wave height) along the damping layer. This indicates that the damping layer can absorb the reflected wave effectively and the re-flection phenomenon can be ignored.

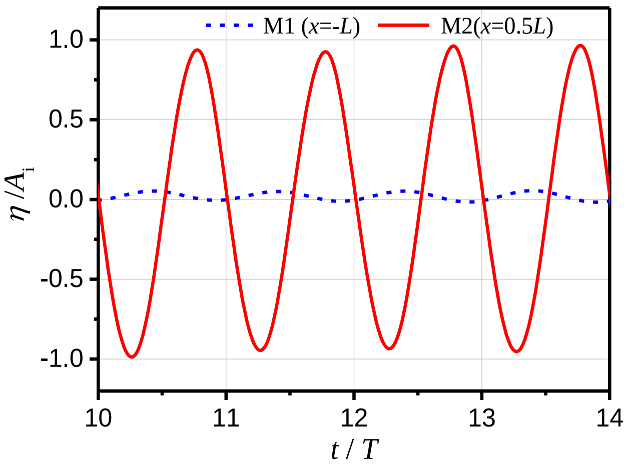

Fig. A1 Time series of surface elevations at different positions in the numerical flume.

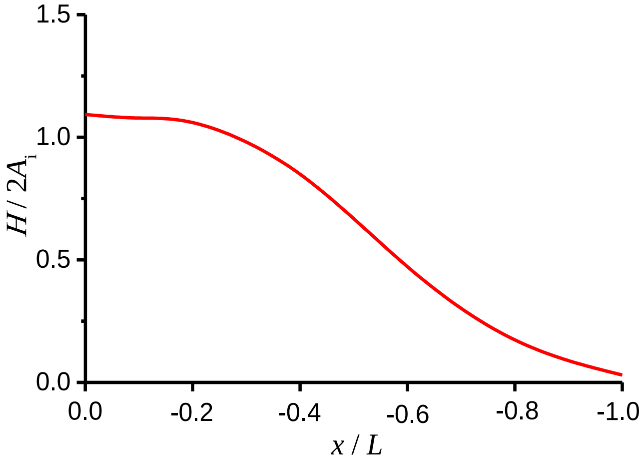

Fig. A2 Wave height distribution along the damping layer.

Appendix B: Determination of the pneumatic damping coefficient C_{dm} and artificial damping coefficient μ_2

The controlling variables method is applied to determine the adaptable pneumatic damping coefficient C_{dm} and artificial damping coefficient μ_2. The same case in Appendix A was taken as an example. Firstly, we set the value of μ_2 as zero and change the value of C_{dm}. Fig. B1 shows that the smallest C_{dm}=7.0 overestimates the surface elevation and underestimates the air pressure, it is vice versa for the largest C_{dm}=12.0. It can be noted that the numerical results are closest to the experimental data for C_{dm}=9.5. Then, the value of C_{dm} is fixed as 9.5 and the value of μ_2 is varied. From Fig. B2 we can see that the existence of viscous damping can reduce the amplitudes of both the surface elevation and air pressure. It can be seen that the numerical results show good agreement with the experimental data for μ_2=0.2. Therefore, the coefficients C_{dm}=9.5 and μ_2=0.2 are determined and the error between the numerical results and experimental data is within 5% with these two conformed parameters. Such trial and error process can be looped until the most adaptable coefficients C_{dm} and μ_2 are obtained.

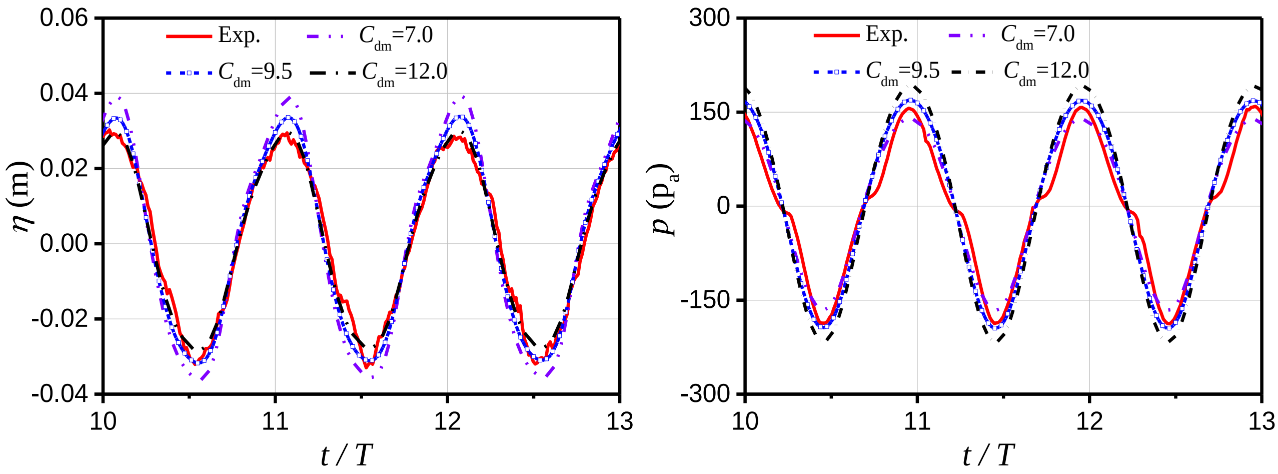

(a) surface elevations (b) air pressure

Fig. B1 Time series of surface elevation at the chamber center and air pressure inside the chamber for different C_{dm} with μ_2 =0.

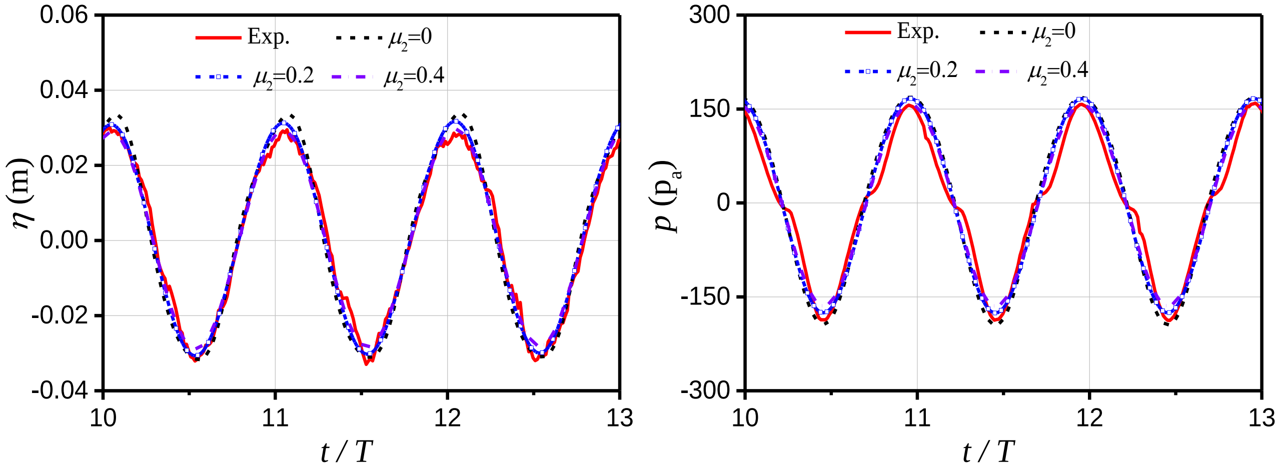

(a) surface elevations (b) air pressure

Fig. B2 Time series of surface elevation at the chamber center and air pressure inside the chamber for different μ_2 with C_{dm} =9.5.

References

[1] Veigas M, López M, Iglesias G. Assessing the optimal location for a shoreline wave energy converter. Appl Energy 2014; 132(11):404-11.

[2] Pinson P, Reikard G, Bidlot JR. Probabilistic forecasting of the wave energy flux. Appl Energy 2012; 93:364-70.

[3] Pontes MT, Falcão AFO. Oceans energies: recourses and utilization. In: Proceedings of the 18th World Energy Conference, Buenos Aires; 2001.

[4] Palha A, Mendes L, Fortes J, Brito-Melo A, Sarmento AJNA. The impact of wave energy farms in the shoreline wave climate: Portuguese pilot zone case study using Pelamis energy wave devices. Renew Energy

2010;35:62-77.

[5] Carballo R, Iglesias G. Wave farm impact based on realistic wave-WEC interaction. Energy 2013;51:216-29.

[6] Falcão AFO. Wave energy utilization: A review of the technologies. Renewable and sustainable energy reviews 2010; 14(3):899-918.

[7] Delauré YMC, Lewis A. 3D hydrodynamic modelling of fixed oscillating water column wave power plant by a boundary element method. Ocean Eng 2003;30(3):309-30.

[8] Morris-Thomas MT, Irvin RJ, Thiagarajan AP. An investigation into the hydrodynamic efficiency of an oscillating water column. J Offshore Mech Arct Eng 2007;129(4):273-8.

[9] Teixeira PRF, Davyt DP, Didier E, Ramalhais R. Numerical simulation of an oscillating water column device using a code based on Navier-Stokes equations. Energy 2013;61:513-30.

[10] Iturrioz A, Guanche R, Armesto JA, et al. Time-domain modeling of a fixed detached oscillating water column towards a floating multi-chamber device. Ocean Eng 2014;76:65-74.

[11] McCormick ME. A modified linear analysis of a wave-energy conversion buoy. Ocean Eng 1976;3:133-44.

[12] Evans DV. The oscillating water column wave energy device. IMA J Appl Math 1978;22(4):423-33.

[13] Falcão AFO, Sarmento AJNA. Wave generation by a periodic surface pressure and its application in wave-energy extraction. In: 15th international congress of theoretical and applied mechanics, Toronto 1980.

[14] Evans DV. Wave-power absorption by systems of oscillating surface pressure distributions. J Fluid Mech 1982;114:481-99.

[15] Falnes J, McIver P. Surface wave interactions with systems of oscillating bodies and pressure distributions. Appl Ocean Res 1985;7:225-34.

[16] Count BM, Evans DV. The influence of projecting sidewalls on the hydrodynamic performance of wave-energy devices. J Fluid Mech 1984;145:361-76.

[17] Wang DJ, Katory M, Li YS. Analytical and experimental investigation on the hydrodynamic performance of onshore wave-power devices. Ocean Eng 2002;29:871-85.

[18] Josset C, Clément AH. A time-domain numerical simulator for oscillating water column wave power plants. Renew Energy 2007;32:1379-402.

[19] Nunes G, Valério D, Beirão P, Sá da Costa J. Modelling and control of a wave energy converter. Renew Energy 2011;36:1913-21.

[20] Falcão AFO, Henriques JCC, Cândido JJ. Dynamics and optimization of the OWC spar buoy wave energy converter. Renew Energy 2012;48:369-81.
[21] Gkikas GD, Athanassoulis GA. Development of a novel nonlinear system identification scheme for the pressure fluctuation inside an oscillating water column-wave energy converter Part I: Theoretical background and harmonic excitation case. Ocean Eng 2014;80:84-99.
[22] Ning DZ, Shi J, Zou QP, Teng B. Investigation of hydrodynamic performance of an OWC (oscillating water column) wave energy device using a fully nonlinear HOBEM (higher-order boundary element method). Energy 2015;83:177-88.
[23] Rezanejad K, Bhattacharjee J, Soares CG. Analytical and numerical study of dual-chamber oscillating water columns on stepped bottom. Renew Energy 2015;75: 272-82.
[24] Marjani AE, Ruiz FC, Rodriguez MA, Santos MTP. Numerical modelling in wave energy conversion systems. Energy 2008;33:1246-53.
[25] Zhang Y, Zou QP, Greaves D. Air-water two-phase flow modeling of hydrodynamic performance of an oscillating water column device. Renew Energy 2012;41:159-70.
[26] López I, Pereiras B, Castro F, Iglesias G. Optimization of turbine-induced damping for an OWC wave energy converter using a RANS-VOF numerical model. Appl Energy 2014;127:105-14.
[27] Luo Y, Nader JR, Cooper P, Zhu SP. Nonlinear 2D analysis of the efficiency of fixed Oscillating Water Column wave energy converters. Renew Energy 2014;64: 255-65.
[28] Iturrioz A, Guanche R, Lara JL, et al. Validation of OpenFOAM® for Oscillating Water Column three-dimensional modeling. Ocean Eng 2015;107:222-36.
[29] Tseng RS, Wu RH, Huang CC. Model study of a shoreline wave-power system. Ocean Eng 2000;27:801-21.
[30] Boccotti P, Filianoti P, Fiamma V, Arena F. Caisson breakwaters embodying an OWC with a small opening-Part II: A small-scale field experiment. Ocean Eng 2007;34:820-41.
[31] Gouaud F, Rey V, Piazzola J, et al. Experimental study of the hydrodynamic performance of an onshore wave power device in the presence of an underwater mound. Coast Eng 2010;57(11): 996-1005.
[32] Liu Z. Experimental and numerical investigation of oscillating water column wave energy convertor. PhD. Thesis. Qingdao: Ocean University of China; 2008.
[33] Dizadji N, Sajadian S.E. Modeling and optimization of the chamber of OWC system. Energy 2011;36:2360-66.

[34] He F, Huang Z, Law W K. An experimental study of a floating breakwater with asymmetric pneumatic chambers for wave energy extraction. Appl Energy 2013; 106(11):222–31.

[35] Imai A, Nagata S, Murakami T, Takao M, Setoguchi T. Experimental study of the generating efficiency of a fixed oscillating water column type wave energy converter. In: Proceedings of the Twenty-fifth (2015) International Ocean and Polar Engineering Conference. International Society of Offshore and Polar Engineers, 2015: 843-48. [Hawaii, USA]

[36] Monk K. Forecasting for control and environmental impacts of wave energy converters. PhD. Thesis. Plymouth University; 2015.

[37] Brendmo A, Falnes J, Lillebekken PM. Linear modelling of oscillating water columns including viscous loss. Appl Ocean Res 1996;18:65-75.

[38] Kim YW. Artificial damping in water wave problems I: Constant Damping. Int J Offshore Polar 2003; 13(2),88-93.

[39] Chen XB. Hydrodynamic analysis for offshore LNG terminals. The Second International Workshop on Applied Offshore Hydrodynamics 2005; Rio de Janeiro, Brazil.

[40] Lu L, Cheng L, Teng B, Zhao M. Numerical investigation of fluid resonance in two narrow gaps of three identical rectangular structures. Appl Ocean Res 2010; 32(2),177-19

[41] López I, Pereiras B, Castro F, Iglesias G. Performance of OWC wave energy converters: influence of turbine damping and tidal variability. Int J Energy Res 2014; 39:472-483.

[42] Veer RV, Thorlen HJ. Added resistance of moonpools in calm water. In: Proceedings of the ASME 27th International Conference on Offshore Mechanics and Arctic Engineering; 2008 [Estoril, Portugal].

[43] He F, Huang Z. Hydrodynamic performance of pile-supported OWC-type structures as breakwaters: An experimental study. Ocean Eng 2014;88:618-26.

[44] Ashlin SJ, Sannasiraj SA and Sundar V. Performance of an oscillating water column device with different bottom profiles subjected to random waves. The 11th International Conference on Hydroscience & Engineering; 2014 [Hamburg, German]

[45] Liu C, Huang Z, Keung ALW, et al. A numerical study of wave energy converter in the form of an oscillating water column based on a mixed Eulerian-Lagrangian formulation. In: Proceedings of the ASME 2010 29th International Conference on Ocean, Offshore and Arctic Engineering. American Society of Mechanical